



Contents lists available at ScienceDirect

Journal of Quantitative Spectroscopy & Radiative Transfer

journal homepage: www.elsevier.com/locate/jqsrt

Extreme Scattering Effect: Light scattering analysis via the Discrete Sources Method

Yuri Eremin^{a,*}, Elena Eremina^{b,1}, Natalia Grishina^a, Thomas Wriedt^{c,2}^a Moscow Lomonosov State University, Lenin's Hills, 119991 Moscow, Russia^b Universitaet Bremen, Badgasteiner Str. 3, 28359 Bremen, Germany^c Institut für Werkstofftechnik, Badgasteiner Str. 3, 28359 Bremen, Germany

ARTICLE INFO

Available online 24 December 2010

Keywords:

Evanescence wave scattering
Gold film
Nano-sized inhomogeneity
Discrete Sources Method
Plasmon Resonance

ABSTRACT

The effect of the Extraordinary Optical Transmission (Ebbesen et al. Nature 1998; 391, 667) through subwavelength holes array in noble metal screen is used for multiple practical applications in nanooptics and biophotonics. In this paper the Extreme Transmission Effect (Eremina et al. Opt. Comm. 2008; 281, 3581) in the noble metal film deposited on a glass prism in the evanescent wave's area is in focus. The Discrete Sources Method (DSM) has been adjusted to calculate the polarized light scattering by an axially symmetric inclusion located in a film deposited on a glass prism. We extended the DSM for the evaluation of the Scattering Cross-Section in the prism domain. It has been shown that the maximum value of the Reflection Cross-Section appears at the same incident angle as for the Transmission Cross-Section. It has been demonstrated that the Reflection Cross-Section can exceed the Transmission Cross-Section under certain circumstances. Analysis of the correlation between the Plasmon Resonance in the gold film and the Extreme Scattering Effect demonstrates that the Plasmon Resonance plays an important but not the exclusive role in the appearance of the Extreme Scattering Effect.

© 2010 Elsevier Ltd. All rights reserved.

1. Introduction

Since the effect of Extraordinary Optical Transmission through arrays of subwavelength holes in metal screens has been detected by Ebbesen et al. [1] it attracted considerable interest by numerous research groups. The ability to localize light in spots much smaller than the volume predicted by diffraction theory offers multiple practical applications in nanooptics and biophotonics. In the paper of Wannemacher [2] this effect has been explained by plasmons excitation. It is now generally agreed that Plasmon Resonance plays a key role

in the enhancement of the light transmission through subwavelength apertures in noble metal screens [3–9]. Recently different scientific teams worldwide have examined the transmission properties of subwavelength apertures in connection with the development of multiple practical applications in nanooptics [10–15].

In our recent paper [16] the effect of extreme light transmission through a nanohole in a noble metal film on a glass prism surface has been reported. The Extreme Transmission Effect differs from the Extraordinary Optical Transmission. The main differences are that it appears in the evanescent wave area only; the Transmission Cross-Section (TCS) connected to the Extreme Transmission Effect under certain "optimal incident angle" beyond the critical one exceeds at an order the TCS under normal excitation, which is usually used in connection with Extraordinary Optical Transmission; besides, the TCS in the Extreme Transmission Effect is extremely sensitive to the change

* Corresponding author. Tel./fax: +7 495 939 1776.

E-mail addresses: eremin@cs.msu.su (Y. Eremin),
eremina@iwt.uni-bremen.de (E. Eremina),
thw@iwt.uni-bremen.de (T. Wriedt).

¹ Tel.: +49 421 218 3583; fax: +49 421 218 5378.² Tel.: +49 421 218 3583; fax: +49 421 218 2507.

of the incident angle and varies up to two orders under variation in the incident angle by just 1.5° . It was found that the Extreme Transmission Effect itself does not depend on the metal film's thickness, hole's diameter and its filling, but it is strongly influenced by the metal film material. In the consecutive papers it was found that the Extreme Transmission Effect occurs not only for hole but also for other types of the film inhomogeneities [17–19].

For three-dimensional light scattering simulation accurate modeling requires an appropriate choice of the method. Since the most interesting nanoeffects are based on resonances, the corresponding computer model must be based on rigorous Maxwell theory. There are multiple approaches, which have been applied to light scattering analysis: Finite Difference Time Domain (FDTD) [20], Finite Element Method (FEM) [21], Coupled Dipole Approximation [22], Volume Integral Equation (VIE) [23], Multiple MultiPole Technique (MMP) [24], Null Field Method [25] and Discrete Sources Method (DSM) [26]. However, most of these methods have different characteristics, restrictions and advantages. The advantage of pure numerical methods, such as the FDTD or the FEM, is the simplicity of implementation. They are applied directly to Maxwell equations. There was a strong trend toward FDTD solvers in the last decades. FDTD is a simple technique, because it does not require profound knowledge of the Maxwell theory. It is based on simple mathematical operations, which can be handled even by very simple computers. Time domain formulations have big advantages when non-linear materials are present, but they are not really well suited for dispersive materials with strong nonlinearities in their frequency response. These models are not accurate enough in many cases [27]. In addition, a conventional FDTD scheme does not account for infinite plane interfaces or uses special trick to approximate it [28]. The simplest way to get rid of problems connected with materials dispersion or strong skin effects near the metal films is to work in the frequency domain. This approach leads to direct methods, such as the FEM. The FEM implementation leads to matrix equations with large sparse matrices. The approach allows to reach a very high accuracy, which is valuable when one explores nanostructures that have not been fabricated yet. However direct application of the FEM to structures with plasmonic features can cause problems related to the truncation of the simulation domain [29].

Other approaches mentioned above are commonly known as semi-analytical methods. This means that one has already applied the Green theorem to the system of Maxwell equations and reduced the scattering problem formulated in whole 3D space to the impurity domain. These methods can be divided into two categories: the volume based methods similar to DDA [30] and VIE, which are suitable for modeling of light scattering by arbitrary impurities, and the surface based methods like MMP, Null Field Method and DSM. While volume based methods can handle any kind of inhomogeneities, they are pretty time consuming, especially for the evaluation of integrated scattering characteristics. Surface based methods seem to be more appropriate for the examination of homogeneous features deposited near an interface. Among others, the MMP and the DSM have several advantages. First of all

they are semi-analytical meshless methods, which do not require any integration procedure. The MMP and the DSM also provide a unique opportunity for a reliable validation of the results, as the errors can be calculated explicitly.

In this paper we adjusted the DSM to analyze polarized light scattering by an inclusion located in a noble metal film deposited on a glass prism. The DSM was extended to evaluate first the Differential Scattering Cross-Section and the Reflection Cross-Section (RCS) in the prism domain. The theory of the method is presented in the next part of the paper and is followed by the description of the DSM numerical scheme. The numerical results based on the DSM model are presented and discussed in the last part of the paper.

2. DSM scattering model

In this section the DSM outlines are discussed. Assume that the whole space is divided into three domains: air D_0 , film D_f and the glass prism, which is represented as a half-space D_1 . Let the plane Σ_1 separate the film and the prism and the plane Σ_f separates air and the film. An axially symmetric inclusion occupying a certain domain D_i with a smooth boundary ∂D is located inside the film of thickness d , bounded by the planes Σ_1 and Σ_f . We assume that the symmetry axis of the inclusion coincides with the normal direction to Σ_1 . Now we introduce a Cartesian coordinate system $Oxyz$ by choosing its origin O at the prism surface Σ_1 . Let the Oz axis coincide with the symmetry axis of the inclusion and is directed to D_0 . The plane $z=0$ corresponds to the Σ_1 plane (Fig. 1).

Then the mathematical statement of the scattering problem for the scattering field outside D_i and the total field inside D_i can be formulated in the following form:

$$\nabla \mathbf{H}_\zeta = jk\epsilon_\zeta \mathbf{E}_\zeta; \quad \nabla \mathbf{E}_\zeta = -jk\mu_\zeta \mathbf{H}_\zeta \quad \text{in } D_\zeta, \quad \zeta = 0, 1, f, i$$

$$\begin{aligned} \mathbf{n}_p(\mathbf{E}_i(p) - \mathbf{E}_f^s(p)) &= \mathbf{n}_p \mathbf{E}_f^0(p), \\ \mathbf{n}_p(\mathbf{H}_i(p) - \mathbf{H}_f^s(p)) &= \mathbf{n}_p \mathbf{H}_f^0(p), \end{aligned} \quad p \in \partial D \quad (1)$$

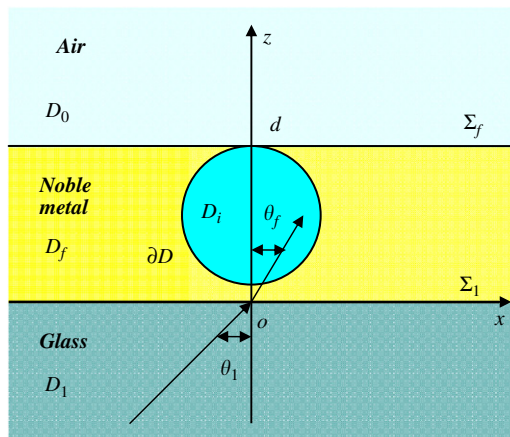


Fig. 1. Model geometry.

$$\begin{aligned} \mathbf{e}_z(\mathbf{E}_f(p) - \mathbf{E}_i(p)) = 0, & \quad \mathbf{e}_z(\mathbf{E}_0(p) - \mathbf{E}_f(p)) = 0 \\ \mathbf{e}_z(\mathbf{H}_f(p) - \mathbf{H}_i(p)) = 0, & \quad \mathbf{e}_z(\mathbf{H}_0(p) - \mathbf{H}_f(p)) = 0 \end{aligned} \quad p \in \Sigma_1; \quad p \in \Sigma_f$$

$$\lim_{r \rightarrow \infty} \left(\sqrt{\varepsilon_\zeta} \mathbf{E}_\zeta^{\mathbf{r}} - \sqrt{\mu_\zeta} \mathbf{H}_\zeta^{\mathbf{z}} \right) = 0, \quad r = |M| \rightarrow \infty, \quad \zeta = 0, 1$$

$$\left(|E_f^s|, |H_f^s| \right) = o(\exp\{-|\text{Im}k_f|\rho\}), \quad \rho = \sqrt{x^2 + y^2} \rightarrow \infty$$

Here, $k = \omega/c$, \mathbf{e}_z is the unit normal vector to the plane $\Sigma_{1,f}$, \mathbf{n}_p is the outward unit normal vector to ∂D , $k = \omega/c$, $\{\mathbf{E}_\zeta, \mathbf{H}_\zeta\}$ is the total field in the corresponding domain $\zeta = 0, 1, f, i$ and $\{\mathbf{E}_\zeta^s, \mathbf{H}_\zeta^s\}$ is an associated scattering field.

Assume that the exciting field $\{\mathbf{E}^0, \mathbf{H}^0\}$ is a linear polarized plane wave propagating from the prism domain D_1 at the angle θ_f with respect to the Z -axis. We start with the solution of the transmission problem of the plane wave $\{\mathbf{E}^0, \mathbf{H}^0\}$ on the layered interface without the inclusion. The result yields fields of external excitation $\{\mathbf{E}_\zeta^0, \mathbf{H}_\zeta^0\}, \zeta = 0, f, 1$ in domains $D_{0,f,1}$, which satisfy the transmission conditions at the planes $\Sigma_{1,f}$. While in $D_{1,f}$ the exciting field consists of the incident and the reflected waves, in D_0 the field includes the transmitted wave, which is transformed into the evanescent one behind the critical angle. In particular, the exciting field in the film can be represented by a linear combination of plane waves propagating up and down inside the film that is

$$\mathbf{E}_f^0 = w_i^{p,S} \mathbf{E}_f^{(+),p,S} + w_r^{p,S} \mathbf{E}_f^{(-),p,S} \mathbf{H}_f^0 = w_i^{p,S} \mathbf{H}_f^{(+),p,S} + w_r^{p,S} \mathbf{H}_f^{(-),p,S} \quad (2)$$

where

$$\mathbf{E}_f^{(\pm),p} = (\mp \cos \theta_f \mathbf{e}_x + \sin \theta_f \mathbf{e}_z) \chi^\pm; \quad \mathbf{H}_f^{(\pm),p} = -n_f \mathbf{e}_y \chi^\pm$$

$$\mathbf{H}_f^{(\pm),s} = n_f (\mp \cos \theta_f \mathbf{e}_x + \sin \theta_f \mathbf{e}_z) \chi^\pm; \quad \mathbf{E}_f^{(\pm),s} = \mathbf{e}_y \chi^\pm$$

$$\chi^\pm = \exp\{-jk_f(x \sin \theta_f \pm z \cos \theta_f)\}; \quad k_\zeta^2 = k^2 \varepsilon_\zeta \mu_\zeta$$

$$n_\zeta = \sqrt{\varepsilon_\zeta \mu_\zeta}, \zeta = 0, f, 1$$

$$w_i^{p,S} = \frac{t_{1f}^{p,S}}{1 - r_{f1}^{p,S} r_{f0}^{p,S} e_f^2}, \quad w_r^{p,S} = -r_{f0}^{p,S} e_f^2 w_i^{p,S}, \quad e_f = \exp\{-jk_f d \cos \theta_f\}$$

Here $r_{v0}^{p,S}$ and $t_{v0}^{p,S}$ are the corresponding coefficients of reflection and transmission at the interface between D_v and D_0 domains, for P - and S -polarized plane waves [31], ε_ζ and μ_ζ are the permittivity and permeability coefficients of the corresponding media, respectively, θ_f is the transmission angle according to Snell's law, $\mathbf{e}_{x,y,z}$ is a Cartesian basis. So, the field $\{\mathbf{E}_f^0, \mathbf{H}_f^0\}$ is the external excitation in (1).

If $\text{Im}(\varepsilon_\zeta, \mu_\zeta) \leq 0$ (the time dependence for the fields was chosen as $\exp(j\omega t)$) and the particle surface is smooth enough: $\partial D \in C^{(2,\infty)}$, then the boundary-value scattering problem described above is uniquely solvable [32].

Following the DSM outlines [33] the approximate solution of the problem (1) is constructed by representing the electromagnetic fields as a finite linear combination of the electric and magnetic fields of dipoles and multipoles distributed over the axis of symmetry inside the scatterer or in an adjoined complex plane. Besides, the fields of multipoles should analytically satisfy the transmission conditions enforced at the plane interfaces $\Sigma_{1,f}$. This circumstance plays the key role because it provides an

opportunity to account for all interactions caused by multiple reflections of the fields between the inclusion and the interface analytically. Then the approximate solution satisfies the Maxwell equations in the domains $D_\zeta, \zeta = 0, 1, f, i$, the infinity conditions and the transmission conditions at the plane interfaces $\Sigma_{1,f}$. Thus, the scattering problem (1) is reduced to the problem of approximation of the exciting field $\{\mathbf{E}_f^0, \mathbf{H}_f^0\}$ at the inclusions surface ∂D . Only the amplitudes of the discrete sources (DS) are to be determined from the boundary conditions at ∂D , which can be written as

$$\begin{aligned} \mathbf{n}_p(\mathbf{E}_i(p) - \mathbf{E}_f^s(p)) = \mathbf{n}_p \mathbf{E}_f^0(p), \\ \mathbf{n}_p(\mathbf{H}_i(p) - \mathbf{H}_f^s(p)) = \mathbf{n}_p \mathbf{H}_f^0(p), \end{aligned} \quad p \in \partial D \quad (3)$$

To construct the fields of dipoles and multipoles that analytically satisfy the transmission conditions at the plane interfaces $\Sigma_{1,f}$ we incorporate Green's Tensor for a layered interface [34]. In the frame of the DSM the approximate solution of the scattering problem is constructed taking into account additionally the rotational symmetry of the scattering problem geometry (axial symmetric inclusion together with the layered interface) and the polarization of the exciting field [33].

Let us start with P -polarized excitation. To account for the axial symmetry and the polarization of the exciting field we incorporate a resolution of the plane wave (2) into a Fourier series with respect to the azimuth angle φ :

$$\begin{aligned} \exp\{-jk_f \rho \sin \theta_f \cos \varphi\} \\ = \sum_{m=0}^{\infty} (2 - \delta_{0m}) (-j)^m J_m(k_f \rho \sin \theta_f) \cos m\varphi \end{aligned}$$

Here $J_m(\cdot)$ is the cylindrical Bessel function and δ_{0m} is Kronecker symbol. Then for the Fourier harmonics of the external excitation in the cylindrical coordinate system (ρ, φ, z) the following representation holds:

$$\begin{aligned} \mathbf{e}_{f(m)}^0 = \{\mathbf{e}_{m\rho}^{0,P}(q) \cos(m+1)\varphi; \quad \mathbf{e}_{m\varphi}^{0,P}(q) \sin(m+1)\varphi; \\ \mathbf{e}_{mz}^{0,P}(q) \cos(m+1)\varphi\} \\ \mathbf{h}_{f(m)}^0 = \{\mathbf{h}_{m\rho}^{0,P}(q) \sin(m+1)\varphi; \quad \mathbf{h}_{m\varphi}^{0,P}(q) \cos(m+1)\varphi; \\ \mathbf{h}_{mz}^{0,P}(q) \sin(m+1)\varphi\} \end{aligned} \quad (4)$$

where $q = (\rho, z)$ stands for a point located in the half plane $\varphi = \text{constant}$. To take the polarization of the external excitation into account we use a linear combination of electrical and magnetic multipoles deposited along the axis of symmetry [33]. For the scattered field representation outside D_i the following vector potentials are used:

$$\begin{aligned} \mathbf{A}_{mn}^{e,\zeta} = \{g_m^e(q, w_n) \cos(m+1)\varphi; \quad -g_m^e(q, w_n) \sin(m+1)\varphi; \\ -f_{m+1}(q, w_n) \cos(m+1)\varphi\} \\ \mathbf{A}_{mn}^{h,\zeta} = \{g_m^h(q, w_n) \sin(m+1)\varphi; \quad g_m^h(q, w_n) \cos(m+1)\varphi; \\ -f_{m+1}(q, w_n) \sin(m+1)\varphi\} \\ \mathbf{A}_n^{e,\zeta} = \{0; \quad 0; \quad g_0^h(q, w_n)\}; \quad \zeta = 0, f, 1 \end{aligned} \quad (5)$$

Here the Fourier harmonics of the Green Tensor $g_m^{e,h}, f_m$, which accept the form of the Weyl–Sommerfeld integrals:

$$\begin{aligned} g_m^{e,h}(q, w_n) = \int_0^\infty J_m(\lambda \rho) v_{11}^{e,h}(z, w_n, \lambda) \lambda^{1+m} d\lambda \\ f_m(q, w_n) = \int_0^\infty J_m(\lambda \rho) v_{31}(z, w_n, \lambda) \lambda^{1+m} d\lambda \end{aligned} \quad (6)$$

The multipoles are distributed along the axis of symmetry $w_n \in Oz$ inside D_i or in an adjoined complex plane by setting $w = z' \pm jz''$ as it was introduced in [35].

The spectral functions $v_{11}^{e,h}, v_{31}^{e,h}$ corresponding to (6) are given by

$$v_{11}^{e,h}(z, w_n, \lambda) = \begin{cases} A_{11}^{e,h}(\lambda, w_n, d) \exp\{-\eta_0 |z-d|\}, & z > d \\ \frac{\exp\{-\eta_f |z-w_n|\}}{\eta_f} + B_{11}^{e,h} \exp\{-\eta_f |z-d|\} \\ + C_{11}^{e,h} \exp\{-\eta_f z\}, & d > z > 0 \\ D_{11}^{e,h}(\lambda, w_n, d) \exp\{\eta_1 z\}, & z < 0 \end{cases};$$

$$v_{31}^{e,h}(z, w_n, \lambda) = \begin{cases} A_{31}^{e,h}(\lambda, w_n, d) \exp\{-\eta_0 |z-d|\}, & z > d \\ B_{31}^{e,h} \exp\{-\eta_f |z-d|\} + C_{31}^{e,h} \exp\{-\eta_f z\}, & d > z > 0 \\ D_{31}^{e,h}(\lambda, w_n, d) \exp\{\eta_1 z\}, & z < 0 \end{cases}$$

Here $\eta_\zeta^2 = \lambda^2 - k_\zeta^2$, $k_\zeta^2 = k^2 \varepsilon_\zeta \mu_\zeta$, $\zeta = 0, f$.

The associated spectral coefficients $A_{\alpha\beta}^{e,h}, B_{\alpha\beta}^{e,h}, C_{\alpha\beta}^{e,h}, D_{\alpha\beta}^{e,h}$ are determined from the following one-dimensional transmission conditions imposed at $z=0, d$:

$$[v_{11}^e] = \left[\frac{1}{\mu} \frac{\partial v_{11}^e}{\partial z} \right] = 0, \quad [v_{11}^h] = \left[\frac{1}{\varepsilon} \frac{\partial v_{11}^h}{\partial z} \right] = 0 \left[\frac{1}{\mu} v_{31}^e \right] = 0,$$

$$\left[\frac{1}{\varepsilon \mu} \frac{\partial v_{31}^e}{\partial z} \right] = - \left[\frac{1}{\varepsilon \mu} \right] v_{11}^e, \quad \left[\frac{1}{\varepsilon} v_{31}^h \right] = 0, \quad \left[\frac{1}{\varepsilon \mu} \frac{\partial v_{31}^h}{\partial z} \right] = - \left[\frac{1}{\varepsilon \mu} \right] v_{11}^h$$

Here square brackets $[.]$ stay for the jump of values across the interface. In particular, the equality $v_{31}^e = v_{31}^h$ holds at $d > z > 0$. For the P-polarized total field representation inside the D_i the following vector potentials are to be used [33]:

$$\mathbf{A}_{mn}^{e,i} = \{Y_m(q, w_n^i) \cos(m+1)\varphi; -Y_m(q, w_n^i) \sin(m+1)\varphi; 0\}$$

$$\mathbf{A}_{mn}^{h,i} = \{Y_m(q, w_n^i) \sin(m+1)\varphi; Y_m(q, w_n^i) \cos(m+1)\varphi; 0\}$$

$$\mathbf{A}_n^{e,i} = \{0; 0; Y_0(q, w_n^i)\} \tag{7}$$

Here

$$Y_m(q, w_n^i) = h_m^{(2)}(k_i R_{qw_n^i}) (k_i \rho / R_{qw_n^i})^m$$

$$R_{qw_n^i} = \sqrt{\rho^2 + (z - w_n^i)^2} \text{ and } h_m^{(2)}(.)$$

is spherical Hankel function. Let us emphasize that the sets $\{w_n^i\}$ and $\{w_n\}$ are different and that w_n^i are located outside D_i .

Thus for the scattered fields in $D_{0,f,1}$, which satisfy the transmission conditions at $\Sigma_{1,f}$ and total field inside D_i , the following representation is valid:

$$\mathbf{E}_N^\zeta = \sum_{m=0}^M \sum_{n=1}^{N_m^\zeta} \left\{ p_{mn}^\zeta \frac{j}{k \varepsilon_\zeta \mu_\zeta} \nabla \times \nabla \times \mathbf{A}_{mn}^{e,\zeta} + q_{mn}^\zeta \frac{1}{\varepsilon_\zeta} \nabla \times \mathbf{A}_{mn}^{h,\zeta} \right\}$$

$$+ \sum_{n=1}^{N_0^\zeta} r_n^\zeta \frac{j}{k \varepsilon_\zeta \mu_\zeta} \nabla \times \nabla \times \mathbf{A}_n^{e,\zeta}, \quad \mathbf{H}_N^\zeta = \frac{j}{k \mu_\zeta} \nabla \times \mathbf{E}_N^\zeta(M)$$

$\zeta = 0, f, 1, i; \quad \xi = f, i.$ (8)

The last term in (8) corresponds to vertical electric dipoles because for P-polarization \mathbf{E}_f^0 vector belongs to the incident plane.

We would like to emphasize that following special construction of the DS fields representation for the fields $\{\mathbf{E}_N^\zeta, \mathbf{H}_N^\zeta\}$: (8) in the domains $D_{0,f,1}$ is provided by unitary set of the amplitudes $\{p_{mn}^f, q_{mn}^f, r_n^f\}$.

The approximate solution for the S-polarized excitation can be constructed in a similar way. Taking into account that the Fourier harmonics for the exciting plane wave can be written as

$$\mathbf{e}_{f(m)}^0 = \{ \mathbf{e}_{m\rho}^{0,S}(q) \sin(m+1)\varphi; \mathbf{e}_{m\phi}^{0,S}(q) \cos(m+1)\varphi; \mathbf{e}_{mz}^{0,S}(q) \sin(m+1)\varphi \}$$

$$\mathbf{h}_{f(m)}^0 = \{ \mathbf{h}_{m\rho}^{0,S}(q) \cos(m+1)\varphi; \mathbf{h}_{m\phi}^{0,S}(q) \sin(m+1)\varphi; \mathbf{h}_{mz}^{0,S}(q) \cos(m+1)\varphi \} \tag{9}$$

The following electric and magnetic vector potentials corresponding to the multipoles are used:

$$\mathbf{A}_{mn}^{e,\zeta} = \{ g_m^e(q, w_n) \sin(m+1)\varphi; g_m^e(q, w_n) \cos(m+1)\varphi; -f_{m+1}(q, w_n) \sin(m+1)\varphi \}$$

$$\mathbf{A}_{mn}^{h,\zeta} = \{ g_m^h(q, w_n) \cos(m+1)\varphi; -g_m^h(q, w_n) \sin(m+1)\varphi; -f_{m+1}(q, w_n) \cos(m+1)\varphi \} \tag{10}$$

$$\mathbf{A}_n^{h,\zeta} = \{ 0; 0; g_0^e(q, w_n) \}; \quad \zeta = 0, f, 1$$

The vector potential for the total field inside D_i accept the following form:

$$\mathbf{A}_{mn}^{e,i} = \{ Y_m(q, w_n^i) \sin(m+1)\varphi; -Y_m(q, w_n^i) \cos(m+1)\varphi; 0 \}$$

$$\mathbf{A}_{mn}^{h,i} = \{ Y_m(q, w_n^i) \cos(m+1)\varphi; Y_m(q, w_n^i) \sin(m+1)\varphi; 0 \}$$

$$\mathbf{A}_n^{h,i} = \{ 0; 0; Y_0(q, w_n^i) \} \tag{11}$$

Then for the scattered fields in $D_{0,1,f}$, which satisfy the transmission conditions at $\Sigma_{1,f}$ and the total field inside D_i the following representation is valid:

$$\mathbf{E}_N^\zeta = \sum_{m=0}^M \sum_{n=1}^{N_m^\zeta} \left\{ p_{mn}^\zeta \frac{j}{k \varepsilon_\zeta \mu_\zeta} \nabla \times \nabla \times \mathbf{A}_{mn}^{e,\zeta} + q_{mn}^\zeta \frac{1}{\varepsilon_\zeta} \nabla \times \mathbf{A}_{mn}^{h,\zeta} \right\}$$

$$+ \sum_{n=1}^{N_0^\zeta} r_n^\zeta \frac{j}{k \varepsilon_\zeta \mu_\zeta} \nabla \times \mathbf{A}_n^{h,\zeta}$$

$$\mathbf{H}_N^\zeta = \frac{j}{k \mu_\zeta} \nabla \times \mathbf{E}_N^\zeta(M), \quad \zeta = 0, f, 1, i; \quad \xi = f, i \tag{12}$$

The last term in (12) corresponds to vertical magnetic dipoles because for S-polarization \mathbf{H}_f^0 vector belongs to the incident plane.

Completeness of the functional system of dipoles and multipoles guarantees the convergence of the approximate solutions (8) and (12) to the exact one [36].

3. DSM numerical scheme

In this section a short description of the DSM numerical scheme is presented. As mentioned above, the representations (8) and (12) satisfy all the conditions of the scattering problem (1) except the transmission conditions at the inclusions surface (3). These conditions are used to determine the unknown amplitudes of the DS $\{p_{mn}^\zeta, q_{mn}^\zeta, r_n^\zeta\}$. For this we need to compute the coefficients $\{p_{mn}^f, q_{mn}^f, r_n^f\}_{n=1}^{N_m^f}$ and $\{p_{mn}^i, q_{mn}^i, r_n^i\}_{n=1}^{N_m^i}$ only, due to the fact that by using Green's Tensor we constructed a unitary representation of the field outside D_i with the same amplitudes. Let us remind that the scattering problem geometry is axially symmetric with respect to the Z-axis and the DS can be distributed over the axis of symmetry. To account for the singularities of the scattered field continuation inside the

inclusion we construct an analytic continuation of the DS's positions into the adjoined complex plane $\{w_n\}_{n=1}^{N_m^f}$ [36]. The DSs for the internal field representation $\{w_n^i\}_{n=1}^{N_m^i}$ are placed in the complex plane in such a way that their projections onto the real axis (Oz) do not touch the domain D_i . Therefore, fulfilling the transmission conditions (3) at the surface ∂D can be reduced to a sequential set of 1D transmission problems for the Fourier harmonics of the fields. Thus, instead of matching the fields on the scattering surface (3), we match their Fourier harmonics separately by reducing the approximation problem on the surface ∂D to a set of 1D problems enforced at the inclusion surface generatrix \mathfrak{I} .

There are various numerical schemes for the evaluation of the amplitudes. It has been found that the most stable results can be obtained by combining the Generalized Point-Matching Technique and the method of Pseudo-Solution of corresponding over-determined systems of linear equations [33]. For pseudo-solution we employ Tikhonov regularization in least-square sense [37]. The unknown vector of the DS amplitudes $\{p_{mn}^i, q_{mn}^i, r_n^i\}$ can be determined as a pseudo-solution of the following over-determined systems of linear equations:

$$\mathbf{B}_m \mathbf{p}_m = \mathbf{f}_m, \quad m = 0, \dots, M \quad (13)$$

Here \mathbf{B}_m is a rectangular matrix $\mathbf{B}_m = [B_{ll}^m]$, $l = 1, \dots, 4L$, $l' = 1, \dots, 2(N_m^i + N_m^f)$. It was found that the reasonable ratio between number L of matching points and the number of DS is $2 < L/(N_m^i + N_m^f) < 4$. In this case the vector of unknown amplitudes \mathbf{p}_m has the length of $2(N_m^i + N_m^f)$ and the vector \mathbf{f}_m in the right-hand side has the length of $4L$. As a rule we choose the number of DS for both the internal and the scattered fields ($N_m^f + N_m^i$) depending on the number of Fourier harmonics m . Then we separate the DS for the scattered field N_m^f and the internal one N_m^i following the value of refractive indices of the film and the inclusion. The higher refractive index of the inclusion the more DSs are required.

For P -polarized excitation the linear system (13) can be written as

$$\begin{bmatrix} -\frac{j}{k\epsilon_i\mu_i} W_m^i & \frac{1}{\epsilon_i} X_m^i & \frac{j}{k\epsilon_j\mu_j} W_m^f & -\frac{1}{\epsilon_j} X_m^f \\ -\frac{j}{k\epsilon_i\mu_i} Y_m^i & \frac{1}{\epsilon_i} V_m^i & \frac{j}{k\epsilon_j\mu_j} Y_m^f & -\frac{1}{\epsilon_j} V_m^f \\ \frac{1}{\mu_i} Q_m^i & \frac{j}{k\epsilon_i\mu_i} Q_m^i & -\frac{1}{\mu_j} Q_m^f & -\frac{j}{k\epsilon_j\mu_j} Q_m^f \\ \frac{1}{\mu_i} U_m^i & \frac{j}{k\epsilon_i\mu_i} S_m^i & -\frac{1}{\mu_j} U_m^f & -\frac{j}{k\epsilon_j\mu_j} S_m^f \end{bmatrix} \begin{pmatrix} P_m^i \\ Q_m^i \\ P_m^f \\ Q_m^f \end{pmatrix} = \begin{pmatrix} \mathbf{e}_{f(m)}^0 \cdot \boldsymbol{\tau} \\ \mathbf{e}_{f(m)}^0 \cdot \mathbf{e}_\varphi \\ \mathbf{h}_{f(m)}^0 \cdot \boldsymbol{\tau} \\ \mathbf{h}_{f(m)}^0 \cdot \mathbf{e}_\varphi \end{pmatrix} \quad (14)$$

The first two columns result from the representation of the internal fields and the next two columns result from the representation of the external fields. The first column of the matrix corresponds to the electric multipoles and the second one to the magnetic ones. Rows correspond to the tangential components of the field in the following order: $E_\tau, E_\varphi, H_\tau, H_\varphi$, where $\boldsymbol{\tau}$ is the vector tangential to the generatrix \mathfrak{I} .

An important fact is that there exist simple relations between the matrix components associated to the P and S polarizations:

$$W^P = W^S, \quad Y^P = Y^S, \quad Q^P = Q^S, \quad S^P = S^S, \quad X^P = -X^S, \quad V^P = -V^S, \\ \Omega^P = -\Omega^S, \quad U^P = -U^S$$

This feature enables to solve the problem for P - and S -polarized excitations using the single matrix just doing a simple transformation of the right-hand part and the DS amplitudes of the vectors system (14) for the S -polarization [38].

The elements of the matrices associated to the scattered field accept the following representation:

$$W_m^f = \alpha \left(g_{m+2}^e - \frac{m+1}{\rho} g_{m+1}^e + k_f^2 g_m^e \right) - \beta \frac{\partial g_{m+1}^e}{\partial z} \\ + \alpha \left(-\frac{m+1}{\rho} \frac{\partial f_{m+1}}{\partial z} + \frac{\partial f_{m+2}}{\partial z} \right) - \beta \left(\frac{\partial^2 f_{m+1}}{\partial z^2} + k_f^2 f_{m+1} \right) \\ Y_m^f = -\frac{m+1}{\rho} g_{m+1}^e + k_f^2 g_m^e - \frac{m+1}{\rho} \frac{\partial f_{m+1}}{\partial z} \\ \Omega_m^f = \alpha \frac{\partial g_m^e}{\partial z} + \beta g_{m+1}^e + \alpha \frac{m+1}{\rho} f_{m+1} \\ U_m^f = \frac{\partial g_m^e}{\partial z} + \frac{m+1}{\rho} f_{m+1} - f_{m+2} \\ X_m^f = -\alpha \frac{\partial g_m^h}{\partial z} - \beta g_{m+1}^h - \alpha \frac{m+1}{\rho} f_{m+1} \\ V_m^f = -\frac{\partial g_m^h}{\partial z} - \frac{m+1}{\rho} f_{m+1} + f_{m+2} \\ Q_m^f = \alpha \left(g_{m+2}^h - \frac{m+1}{\rho} g_{m+1}^h + k_f^2 g_m^h \right) - \beta \frac{\partial g_{m+1}^h}{\partial z} \\ + \alpha \left(-\frac{m+1}{\rho} \frac{\partial f_{m+1}}{\partial z} + \frac{\partial f_{m+2}}{\partial z} \right) - \beta \left(\frac{\partial^2 f_{m+1}}{\partial z^2} + k_f^2 f_{m+1} \right) \\ S_m^f = -\frac{m+1}{\rho} g_{m+1}^h + k_f^2 g_m^h - \frac{m+1}{\rho} \frac{\partial f_{m+1}}{\partial z}, \quad \boldsymbol{\tau} = (\alpha, 0, \beta)$$

The matrix for φ independent harmonic for P -polarization has the following form:

$$\begin{bmatrix} -\frac{j}{k\epsilon_i\mu_i} W^i & \frac{j}{k\epsilon_j\mu_j} W^f \\ -\frac{1}{\mu_i} U^i & -\frac{1}{\mu_j} U^f \end{bmatrix}$$

where the first row corresponds to E_τ component and the second corresponds to H_φ one. The matrix elements for scattered field are

$$W^f = \alpha \frac{\partial^2}{\partial \rho \partial z} g_0^h + \beta \left(\frac{\partial^2 g_0^h}{\partial z^2} + k^2 g_0^h \right), \quad U^f = -\frac{\partial g_0^h}{\partial \rho}$$

Similar to the previous case the matrix for the S -polarization accepts the form:

$$\begin{bmatrix} -\frac{1}{\epsilon_i} V^i & \frac{1}{\epsilon_j} V^f \\ \frac{j}{k\epsilon_i\mu_i} Q^i & -\frac{j}{k\epsilon_j\mu_j} Q^f \end{bmatrix}$$

where the first row corresponds to E_φ component and the second to H_τ component. Matrix elements in this case can be presented as

$$V^f = -\frac{\partial g_0^e}{\partial \rho}, \quad Q^f = \alpha \frac{\partial^2}{\partial \rho \partial z} g_0^e + \beta \left(\frac{\partial^2 g_0^e}{\partial z^2} + k^2 g_0^e \right)$$

So, for φ -independent harmonic one has to solve two linear systems independently. Let us remind that the dimension of the systems is twice less than the dimension of (14).

Hence, by solving the linear systems (14) for the whole range of harmonics $m = 0, \bar{M}$, plus two systems for φ

independent harmonics we are able to get the approximate solutions (8) and (12). Besides, the DSM enables to estimate errors of the solution obtained by evaluation of the surface residual by satisfying (3) in the intermediate points with respect to the matching points.

After the amplitudes of the DS are determined, one can compute the far field pattern $\mathbf{F}(\theta, \varphi)$ of the scattered field, which is determined at the unit sphere $\Omega = \{0^\circ \leq \theta < 180^\circ, 0^\circ \leq \varphi \leq 360^\circ\}$ and is given by

$$\mathbf{E}_{0,1}^s(\mathbf{r}) / |\mathbf{E}^0(z=0)| = \frac{\exp\{-jk_0 r\}}{r} \mathbf{F}_{0,1}(\theta, \varphi) + O(r^{-2}) \quad r = |\mathbf{M}| \rightarrow \infty$$

Here $\mathbf{F}_{0,1}(\theta, \varphi) = F_{0,1(\theta)} \mathbf{e}_\theta + F_{0,1(\varphi)} \mathbf{e}_\varphi$.

By asymptotical estimation of the Weyl–Sommerfeld integrals involved in (6) the representation of the elements of the far field pattern takes the form of a finite linear combination of elementary functions [39]:

$$\begin{aligned} F_{0,1(\theta)}^P(\theta, \varphi) &= jk \sum_{m=0}^M (jk_{0,1} \sin \theta)^m \cos(m+1)\varphi \\ &\sum_{n=1}^{N_m^f} \left\{ p_{nm}^{f,P} \bar{g}_{nm}^{e(0,1)} \cos \theta + jk_{0,1} \sin^2 \theta \bar{f}_{nm}^{e(0,1)} \right\} \\ &+ \sqrt{\frac{\mu_{0,1}}{\varepsilon_{0,1}}} q_{nm}^{f,P} \bar{g}_{nm}^{h(0,1)} \left\} - jk \sin \theta \sum_{n=1}^{N_0^f} r_n^{f,P} \bar{g}_{n0}^{h(0,1)} \right. \\ F_{0,1(\varphi)}^P(\theta, \varphi) &= -jk \sum_{m=0}^M (jk_{0,1} \sin \theta)^m \sin(m+1)\varphi \\ &\times \sum_{n=1}^{N_m^f} \left\{ p_{nm}^{f,P} \bar{g}_{nm}^{e(0,1)} + \sqrt{\frac{\mu_{0,1}}{\varepsilon_{0,1}}} q_{nm}^{f,P} \left[\bar{g}_{nm}^{h(0,1)} \cos \theta \right. \right. \\ &\left. \left. + jk_{0,1} \sin^2 \theta \bar{f}_{nm}^{h(0,1)} \right] \right\} \quad (15) \end{aligned}$$

For S-polarized external excitation the components of the far field pattern accept the following form:

$$\begin{aligned} F_{0,1(\theta)}^S(\theta, \varphi) &= jk \sum_{m=0}^M (jk_{0,1} \sin \theta)^m \sin(m+1)\varphi \\ &\sum_{n=1}^{N_m^f} \left\{ p_{nm}^{f,S} \bar{g}_{nm}^{e(0,f)} \cos \theta + jk_{0,f} \sin^2 \theta \bar{f}_{nm}^{e(0,f)} \right\} \\ &- \sqrt{\frac{\mu_{0,f}}{\varepsilon_{0,f}}} q_{nm}^{f,S} \bar{g}_{nm}^{h(0,f)} \left\} \right. \\ F_{0,1(\varphi)}^S(\theta, \varphi) &= jk \sum_{m=0}^M (jk_{0,1} \sin \theta)^m \cos(m+1)\varphi \\ &\sum_{n=1}^{N_m^f} \left\{ p_{nm}^{f,S} \bar{g}_{nm}^{e(0,1)} - \sqrt{\frac{\mu_{0,1}}{\varepsilon_{0,1}}} q_{nm}^{f,S} \left[\bar{g}_{nm}^{h(0,1)} \cos \theta \right. \right. \\ &\left. \left. + jk_{0,1} \sin^2 \theta \bar{f}_{nm}^{h(0,1)} \right] \right\} + jk \sqrt{\frac{\mu_{0,1}}{\varepsilon_{0,1}}} \sin \theta \sum_{n=1}^{N_0^f} r_n^{f,S} \bar{g}_{nm}^{e(0,1)} \left. \right. \\ F_{0,1(\varphi)}^S(\theta, \varphi) &= jk \sum_{m=0}^M (jk_{0,1} \sin \theta)^m \cos(m+1)\varphi \\ &\sum_{n=1}^{N_m^f} \left\{ p_{nm}^{f,S} \bar{g}_{nm}^{e(0,1)} - \sqrt{\frac{\mu_{0,1}}{\varepsilon_{0,1}}} q_{nm}^{f,S} \left[\bar{g}_{nm}^{h(0,1)} \cos \theta \right. \right. \\ &\left. \left. + jk_{0,1} \sin^2 \theta \bar{f}_{nm}^{h(0,1)} \right] \right\} + jk \sqrt{\frac{\mu_{0,1}}{\varepsilon_{0,1}}} \sin \theta \sum_{n=1}^{N_0^f} r_n^{f,S} \bar{g}_{nm}^{e(0,1)} \quad (16) \end{aligned}$$

Here $\{p_{nm}^{f,(P,S)}, q_{nm}^{f,(P,S)}, r_n^{f,(P,S)}\}$ are Fourier harmonics of the DS amplitudes corresponding to P/S excitations and the associated spectral functions $\bar{g}_{nm}^{e,h}, \bar{f}_{nm}^{e,h}$ have the form:

$$\begin{aligned} \bar{g}_{nm}^{e,h(0)}(\theta) &= jk_0 \cos \theta \exp\{jk_0 d \cos \theta\} A_{11}^{e,h}(k_0 \sin \theta, w_n, d) \\ \bar{f}_{nm}^{e,h(0)}(\theta) &= jk_0 \cos \theta \exp\{jk_0 d \cos \theta\} A_{31}^e(k_0 \sin \theta, w_n, d) \\ \bar{g}_{nm}^{e,h(1)}(\theta) &= jk_1 \cos \theta D_{11}^{e,h}(k_1 \sin \theta, w_n, d) \\ \bar{f}_{nm}^{e,h(1)}(\theta) &= jk_1 \cos \theta D_{31}^{e,h}(k_1 \sin \theta, w_n, d) \end{aligned}$$

Hence, after the unknown amplitudes of DS are determined, the far field patterns for P- and S-polarized excitations are represented as finite linear combinations of elementary functions. This circumstance ensures fast and effective computer analysis of scattering characteristics in the far zone.

3.1. Results and discussion

In this section we discuss the results of computer simulations for the inclusion deposited inside a gold film. We analyze the Differential Scattering Cross-Section (DSC), which is given by

$$DSC_{0,1}^{P,S}(\theta_1, \theta, \varphi) = \left| F_{0,1(\theta)}^{P,S}(\theta_1, \theta, \varphi) \right|^2 + \left| F_{0,1(\varphi)}^{P,S}(\theta_1, \theta, \varphi) \right|^2 \quad (17)$$

Here the components of far field pattern are given by (15) and (16). The dimension of $DSC_{0,1}^{P,S}$ is μm^2 units. We also examine the Scattering Cross-Sections (CS) in the upper and lower semi-spheres, which represents the integrated intensity scattered into the prescribed solid angle Ω :

$$\sigma_{0,1}^{P,S}(\theta_1) = \int_{\Omega_{0,1}} DSC_{0,1}^{P,S}(\theta_1, \theta, \varphi) d\omega \quad (18)$$

where the solid angle $\Omega_0 = \{0^\circ \leq \theta \leq 180^\circ, 0^\circ \leq \varphi \leq 360^\circ\}$ corresponds to the TCS and $\Omega_1 = \{90^\circ \leq \theta \leq 180^\circ, 0^\circ \leq \varphi \leq 360^\circ\}$ corresponds to the RCS.

Let θ_0 be a transmission angle of the plane wave in D_0 . Snell's law in this case results $\sin \theta_0 = (n_1/n_0) \sin \theta_1$. As $|n_1| > |n_0|$ with increase in incident angle θ_1 from 0 till $\pi/2$ yields $|\sin \theta_0| > 1$. This fact requires using a corresponding

branch of $\cos \theta_0 = -j\sqrt{\sin^2 \theta_0 - 1}$, which assures an outgoing wave. Hence, beyond the critical angle $\theta_c = \arcsin(n_0/n_1)$ in the upper half-space an evanescent wave appears, which propagates along the interface and damps in the normal ($z > d$) direction to the interface Σ_f :

$$\chi^+ = \exp\{-jk_0 x \sin \theta_0\} \exp\{-k_0 z \sqrt{\sin^2 \theta_0 - 1}\}.$$

The plasmon resonance corresponds to the minimum value of the reflection coefficient R_{01}^P with respect to the incident angle θ_1 of the plane wave from Σ_1 interface. It appears in the evanescent wave area for P-polarized excitation only [40]

$$R_{01}^P(\theta_1) = \frac{r_{1f}^P + r_{f0}^P \exp\{-2jk_f \cos \theta_f d\}}{1 + r_{1f}^P r_{f0}^P \exp\{-2jk_f \cos \theta_f d\}} \quad (19)$$

Now we present some numerical results obtained by using the DSM model. We use an exciting wavelength of $\lambda = 633$ nm, the prism material is glass N-LASF46A with the refractive index $n_1 = 1.898$. In this case the critical angle is $\theta_c = \arcsin(1/1.898) \cong 31.79^\circ$. We use a gold film of

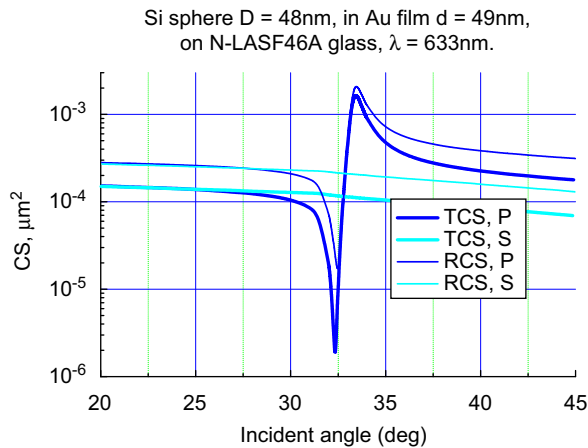


Fig. 2. TCS and RCS (18) for a silicon spherical inclusion of $D=48$ nm in a gold film of $d=49$ nm for P - and S -polarizations versus incident angle.

thickness d and the refractive index $n_f=0.183 - 3.433j$ [41]. All refractive indices were taken from the open sources [42]. We consider two types of inclusions located inside the film: a spherical particle of $D=48$ nm and a cylinder of $D=48$ nm and $h=49$ nm. Inclusion material is silicon ($n_i=3.969 - 0.056j$).

Computations were performed on laptop with a 2.14 GHz CPU (Core 2 Duo) and 2 GB of RAM. For the case of sphere of $D=48$ nm it takes 230 s including 280 incident angles of P/S -polarized plane wave (high resolution is required near plasmon resonance) and integration over the upper (TCS) and lower (RCS) hemi-spheres.

In Fig. 2 the numerical results for both the TCS and the RCS (18) for a silicon sphere of $D=48$ nm in a gold film of $d=49$ nm for P - and S -polarizations versus incident angle are presented.

From the results we can see that both curves for P -polarized excitation demonstrate sharp minima directly beyond the critical angle 31.79° and then maxima in the evanescent waves region. On contrary, the curves for S -polarized light demonstrate monotonic behavior without any jumps of values. The results for the DSC (17) versus scattering angle in the plane of the incidence for the same particle are presented in Fig. 3.

Here the angles region $90-270^\circ$ belongs to the prism area and is responsible for the RCS and the angles region $270-90^\circ$ belongs to the upper half-space and is responsible for the TCS. Two of three curves presented in Fig. 3 correspond to incident angles where the TCS and the RCS demonstrate their minimum ($\theta_1=32.0^\circ$) and maximum ($\theta_1=33.4^\circ$) values (see Fig. 2), the third one describes normal incidence ($\theta_1=0^\circ$). From these results we observe a drastic difference in values of the DSC depending on the incident angles. In addition, if in the upper semi-plane all curves are smooth and do not demonstrate any special features, in the lower semi-plane all of them demonstrate maxima and minima near the incident and the specular directions.

Similar results are presented in Figs. 4 and 5 but for another type of inclusion. Here we have a cylindrical silicon inclusion of $D=48$ nm in a gold film of $d=49$ nm. In general, the behavior of the TCS and the RCS curves is similar to

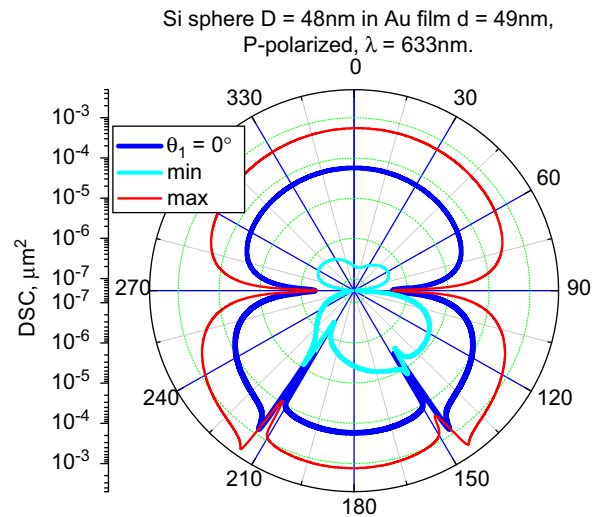


Fig. 3. DSC (17) versus scattering angle for the spherical inclusion of $D=48$ nm in a gold film of $d=49$ nm for different incident angle values.

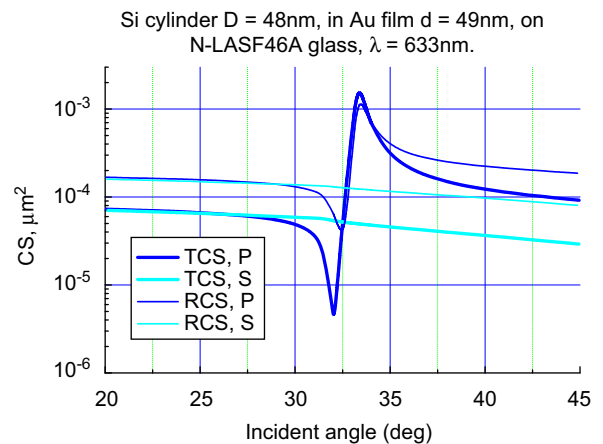


Fig. 4. TCS and RCS for the silicon cylindrical inclusion of $D=48$ nm in a gold film of $d=49$ nm for P - and S -polarizations.

those we observed in Figs. 2 and 3. From these figures we can conclude that the general behavior of the effect we observe does not depend on the inclusion shape. The latter circumstance allows to rename the Extreme Transmission Effect into the Extreme Scattering Effect.

Next we would like to investigate the relation between the thickness of the film and the behavior of the TCS. In Fig. 6 the results for the spherical silicon inclusions of $D=48$ nm for P -polarized light are presented for two values of the film thickness: $d=49$ and 60 nm. The inclusions are attached to the upper surface of the film. From these results we can conclude that despite some variations in the intensity, the positions of the maxima for all curves stay nearly the same. Similar results are presented in Fig. 7 for the cylindrical inclusions of $D=48$ nm in the same gold films as in Fig. 6. The results confirm our previous observations.

In Fig. 8 the results for the TCS of spherical and cylindrical silicon inclusions of $D=48$ nm in films with

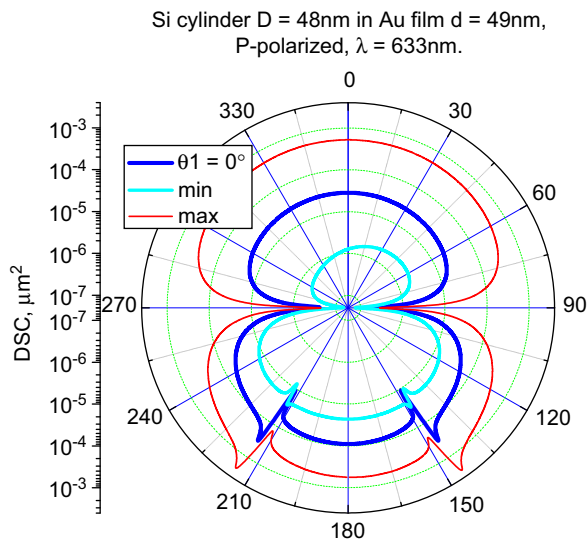


Fig. 5. DSC versus scattering angle for the cylindrical inclusion of $D=48$ nm in a gold film of $d=49$ nm for different incident angle values.

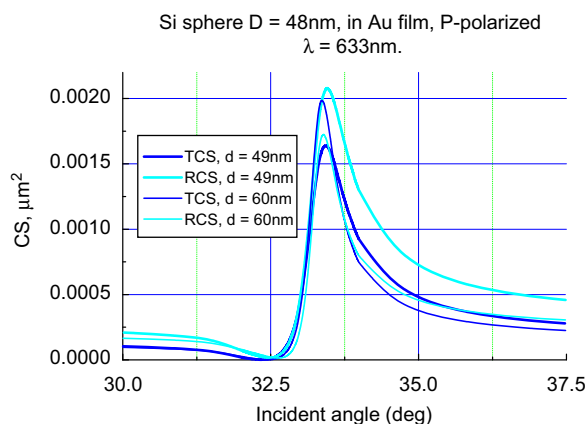


Fig. 6. TCS and RCS for the spherical inclusion of $D=48$ nm in gold films of different thicknesses for P -polarization.

thicknesses $d=49$ and 60 nm for P -polarized light are presented. We can see that the TCS for the spherical inclusion is higher than for the cylindrical one in spite the volume of the sphere is less than the volume of the cylinder. However the position of maxima of all the curves stays almost the same. In addition, while the maximum value for the spherical particles increases with respect to the film thickness, for the cylindrical ones it drops.

Fig. 9 demonstrates the DSC in the incident plane versus scattering angle for the same inclusions as before for the fixed incident angle corresponding to the maximum value of the TCS curves from Fig. 8. From the results presented in Fig. 9 we can observe that despite the close values of all the curves in the upper half-space, the values of maxima and minima of the curves in the prism area differ essentially.

Let us now examine the ratio between the TCS and the RCS for the silicon inclusion of the same size as before in the films of different thicknesses. In Fig. 10 the results for TCS/RCS ratio versus incident angle are presented for the

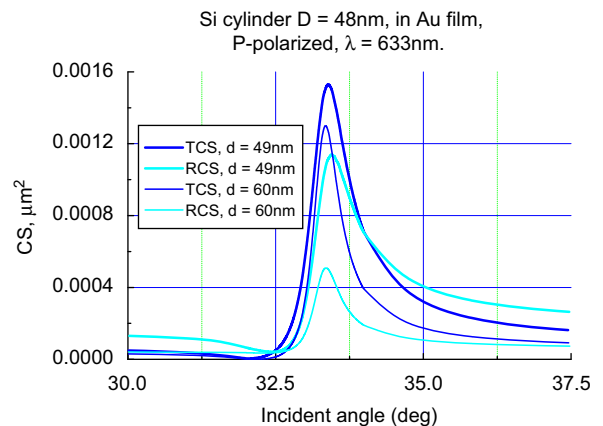


Fig. 7. TCS and RCS for the cylindrical inclusions of $D=48$ nm in gold films of different thicknesses for P -polarization.

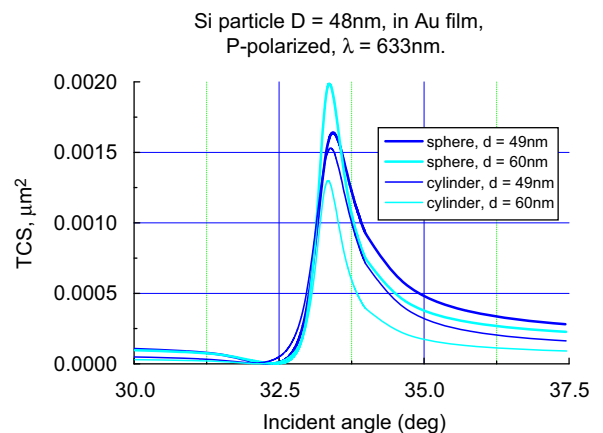


Fig. 8. TCS for silicon inclusions of different shapes of $D=48$ nm in gold films of different thicknesses for P -polarization.

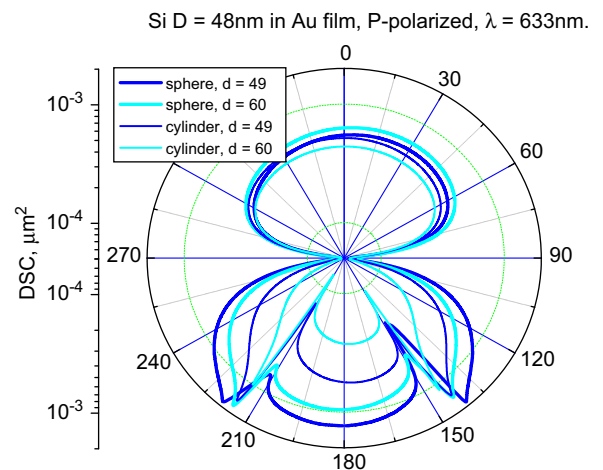


Fig. 9. DSC versus scattering angle for silicon inclusions of different shapes of $D=48$ nm in gold films of different thicknesses for P -polarization.

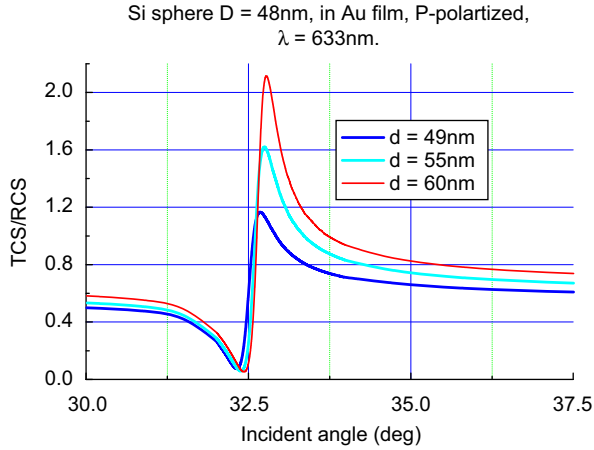


Fig. 10. Ratio TCS/RCS for the spherical inclusions of $D=48$ nm in gold films of different thicknesses for P -polarization.

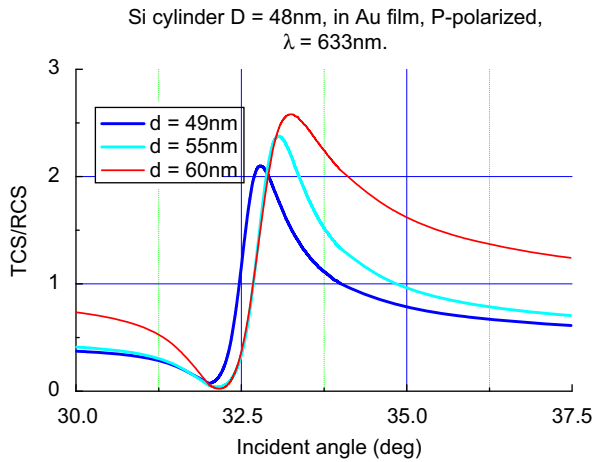


Fig. 11. Ratio TCS/RCS for the cylindrical inclusions of $D=48$ nm in gold films of different thicknesses for P -polarization.

spherical inclusion and in Fig. 11 similar results are presented for the cylindrical one. From the results presented above we can conclude that with increase in the film thickness the TCS value becomes higher than the value of the RCS, especially in the area of maxima.

Now consider a correlation between the plasmon resonance with the Extreme Scattering Effect. In Fig. 12 the results for the reflection coefficients (19) and the total CS including both the TSC and the RSC ($SCS=TSC+RSC$) are presented for the silicon spherical inclusion in gold films of three different thicknesses. While the SCS curves presented in Fig. 12 show very close maximum values, the curves for the reflection coefficients at the same region of the incident angles differ from each other by two orders or more. The last fact demonstrates that in spite the Extreme Scattering Effect definitely correlates with the plasmon resonance [18–19] it does not completely depends on its intensity. This allows us to conclude that the plasmon resonance plays an important but not the main role in appearance of the Extreme Scattering Effect.

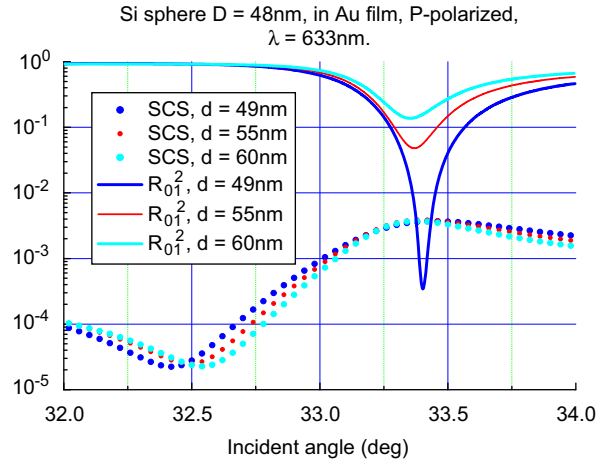


Fig. 12. Reflection coefficients (19) and the total CS for the spherical inclusions of $D=48$ nm in gold films of different thicknesses.

The benefits of the application in the DSM model to this particular task are as follows:

1. It satisfies analytically all conditions of the scattering problem except transmission condition at the inclusion surface.
2. It accounts for axial symmetric geometry of the inclusion which requires to consider just a few the Fourier harmonics (3–4).
3. Generalized Point-Matching Techniques enable to reduce the number of DS up to 3–4 times compared to the Boundary Integral Equation Method.
4. It allows to compute all incident angles and both polarizations at once.
5. It has a reliable criterion for errors of the result evaluation by computing surface residual at the inclusion surface.

4. Conclusion

In this paper the Discrete Sources Method has been adjusted to calculate polarized light scattering by a silicon inclusion located in a noble metal film deposited on a glass prism. We extended Discrete Sources Method to evaluate for the first time the Differential Scattering Cross-Section in the prism domain and the Reflection Cross-Section. It has been shown that the maximum value of the Reflection Cross-Section appears at the same angles as for the Transmission Cross-Section. It was demonstrated that the Reflection Cross-Section can exceed the Transmission Cross-Section under certain circumstances. The latter fact allows to rename the Extreme Transmission Effect into the Extreme Scattering Effect. Analysis of the correlation between the plasmon resonance in the gold film and the Extreme Scattering Effect demonstrates that the plasmon resonance plays an important but not exclusive role in appearance of the Extreme Scattering Effect.

Acknowledgments

We gratefully acknowledge funding of this research by Deutsche Forschungsgemeinschaft (DFG) and the Russian Foundation for Basic Research (RFBR).

References

- [1] Ebbesen TW, Lezec HJ, Ghaemi HF, Thio T, Wolff PA. Extraordinary optical transmission through sub-wavelength hole arrays. *Nature* 1998;391:667–9.
- [2] Wannemacher R. Plasmon-supported transmission of light through nanometric holes in metallic thin films. *Opt Commun* 2001;195:107–18.
- [3] Genet C, Ebbesen TW. Light in tiny holes. *Nature* 2007;225:39–46.
- [4] de Abajo FJG. Colloquium: light scattering by particle and hole arrays. *Rev Mod Phys* 2007;79:1267–90.
- [5] Yin L, Vasko-Vlasov VK, Rydh A, et al. Surface plasmons at single nanoholes in Au films. *Appl Phys Lett* 2004;85(3):467–9.
- [6] Rindzevicius T, et al. Nanohole plasmons in optically thin gold films. *J Phys Chem C* 2007;111(3):1207–12.
- [7] Alegret J, Johansson P, Käll M. Green's tensor calculations of plasmon resonances of single holes and hole pairs in thin gold films. *New J Phys* 2008;10:105004.
- [8] Sepúlveda B, et al. Shape effects in the localized surface plasmon resonance of single nanoholes in thin metal films. *Opt Exp* 2008;16(8):5609–16.
- [9] Baudrion A-L, et al. Coupling efficiency of light to surface plasmon polariton for single subwavelength holes in a gold film. *Opt Exp* 2008;16(5):3420–9.
- [10] Przybilla F, et al. Efficiency and finite size effects in enhanced transmission through subwavelength apertures. *Opt Exp* 2008;16(13):9571–9.
- [11] de León-Pérez F, Brucoli G, García-Vidal FJ, Martín-Moreno L. Theory on the scattering of light and surface plasmon polaritons by arrays of holes and dimples in a metal film. *New J Phys* 2008;10:105017.
- [12] Laux E, Genet C, Ebbesen TW. Enhanced optical transmission at the cut off transition. *Opt Exp* 2009;17(9):6920–30.
- [13] Shuford KL, Gray SK, Ratner MA, Schatz GC. Substrate effects on surface plasmons in single nanoholes. *Chem Phys Lett* 2007;435:123–6.
- [14] Eom GS, Yang D, Lee S, Park S, Lee Y, Hahn JW. Wave propagation characteristics of a figure-eight shaped nanoaperture. *J Appl Phys* 2007;101:103101.
- [15] Zayats AV, Smolyaninov II, Maradudin AA. Nano-optics of surface plasmon polaritons. *Phys Rep* 2005;408:131–4.
- [16] Eremina E, Eremin Y, Grishina N, Wriedt T. Analysis of light scattering in the evanescent waves area by a cylindrical nanohole in a noble-metal film. *Opt Commun* 2008;281:3581–6.
- [17] Eremina E, Eremin Y, Grishina N, Wriedt T. Spectral scattering properties of a nanohole in a noble-metal film in the evanescent waves area. *J Quant Spectrosc Radiat Transfer* 2009;110:1518–25.
- [18] Eremina E, Eremin Y, Grishina N, Wriedt T. Analysis of extreme light transmission through a nanohole in a metal film based on discrete sources method. *J Comput. Theor Nanosci* 2009;6(3):786–803.
- [19] Grishina NV, Eremin YuA, Sveshnikov AG. Analysis of the effect of an extreme energy transmission through a conducting film with a nano-sized inset. *Opt Spectrosc* 2009;106(5):753–6.
- [20] Taflove A, Hagness S. Computational electrodynamics: the finite-difference time-domain method. Norwood: Artech House; 2005.
- [21] Jin J. The finite element method in electromagnetics. Chichester: John Wiley & Sons; 1993.
- [22] Chaumet PC, Rahmani A, Bryant GW. Generalization of the coupled dipole method to periodic structures. *Phys Rev B* 2003;67:165404.
- [23] Søndergaard T. Modeling of plasmonic nanostructures: Green's function integral equation methods. *Phys Status Solidi B* 2007;244(10):3448–62.
- [24] Hafner C. The generalized multiple multipole technique for computational electromagnetics. Boston, MA: Artech House; 1990.
- [25] Doicu A, Wriedt T, Yu Eremin. Light scattering by systems of particles. null-field method with discrete sources – theory and programs. Berlin: Springer Verlag; 2006.
- [26] Eremin YuA. The method of discrete sources in electromagnetic scattering by axially symmetric structures. *J Commun Tech Electron* 2000;45(S2):S269–80.
- [27] Hafner Ch. Boundary methods for optical nano structures. *Phys Status Solidi B* 2007;244(10):3435–47.
- [28] Capoglu IR, Smith GS. A direct time-domain FDTD near-field-to-far-field transform in the presence of an infinite grounded dielectric slab. *IEEE Trans Antennas Propag* 2006;52(12):3805–14.
- [29] Alegret J, Johansson P, Käll M. Green's tensor calculations of plasmon resonances of single holes and hole pairs in thin gold films. *New J Phys* 2008;10:105004.
- [30] Bae E, Zhang H, Hipleman D. Application of discrete dipole approximation for dipoles embedded in film. *J Opt Soc Am A* 2008;25(7):1728–36.
- [31] Chew WC. Waves and fields in inhomogeneous media. NY: IEEE Press; 1995.
- [32] Colton D, Kress R. Inverse acoustic and electromagnetic scattering theory. Berlin: Springer; 1992.
- [33] Eremin YuA, Sveshnikov AG. Mathematical models in nanooptics and biophotonics problems on the base of discrete sources method. *Comput Maths Math Phys* 2007;47(2):262–79.
- [34] Kong JA. Electromagnetic wave theory. Cambridge, MA: EMW Publishing; 2000.
- [35] Eremin YuA. Presentation of fields in terms of sources in the complex plane in the method of nonorthogonal series. *Sov Phys Dokl* 1983;28(6):451–2.
- [36] Doicu A, Yu Eremin, Wriedt T. Acoustic and electromagnetic scattering analysis using discrete sources. London: Academic Press; 2000.
- [37] Morozov VA. Regularization methods for ill-posed problems. London: CRC Press; 1993.
- [38] Grishina NV, Eremin YuA, Sveshnikov AG. Mathematical models of defects of stratified structures based on discrete sources method. *Fundamentalnaya I Prikladnaya Mat* 1998;4(3):1–15 in Russian.
- [39] Eremin YuA, Orlov NV, Sveshnikov AG. Models of electromagnetic scattering problems based on discrete sources methods. In: Wriedt T, editor. Generalizes multipole techniques for electromagnetic and light scattering. Amsterdam: Elsevier Science; 1999. p. 39–79.
- [40] Raether H. Surface plasmon on smooth and rough surfaces and on gratings. Berlin: Springer; 1998 [chapter 2].
- [41] Johnson PB, Christy RW. Optical constants of the noble metals. *Phys Rev B* 1972;6:4370–9.
- [42] <<http://refractiveindex.info>>.